Current-induced dynamics of a monodomain ferromagnet in an external magnetic field applied in easy magnetic plane: Macrospin model

Paul P. Horley,[1,2] Vítor R. Vieira,[2] Peter M. Gorley,[1] Vitalii K. Dugaev,[3] and Józef Barnaś[4,*]

[1]*Department of Physics, Yuri Fedkovych Chernivtsi National University, 2 Kotsyubynsky street, 58012 Chernivtsi, Ukraine*

[2]*Centro de Física das Interacções Fundamentais, Instituto Superior Técnico, Avenida Rovisco Pais, 1049-001 Lisbon, Portugal*

[3]*Department of Mathematics and Applied Physics, Rzeszów University of Technology, Aleja Powstańców Warszawy 6, 35-959 Rzeszów, Poland*

[4]*Institute of Molecular Physics, Polish Academy of Sciences, Smoluchowskiego 17, 60-179 Poznań, Poland*

(Received 24 July 2007; revised manuscript received 26 October 2007; published 25 March 2008)

Numerical results on current-induced magnetization dynamics of a ferromagnet are presented in the framework of a macrospin model. The Landau–Lifshitz–Gilbert equation is used to study the magnetic dynamics for an arbitrary angle between the magnetic field and injected spin-current polarization when they both lie in the easy magnetic plane. It is shown that in some configurations, the magnetic oscillations can reach a significant amplitude (observable via the giant magnetoresistance effect) and frequencies of dozens of gigahertz. Moreover, the model also predicts frequency jumps of the steady magnetization precession.

DOI: 10.1103/PhysRevB.77.094427 PACS number(s): 75.50.Cc, 75.30.Gw, 75.40.Mg, 85.75.−d

I. INTRODUCTION

Spintronics[1] is a rapidly developing area of modern physics and electronics, which makes use of electron spin on equal footing with its charge. There is no doubt that spintronics will lead to smaller electronic devices of increased sensitivity to weak magnetic fields and high operation frequencies. Giant magnetoresistance[2] (GMR)—the effect of a drastic change in electrical resistance due to the magnetization reorientation—allowed enormous advances in information data storage technology, enabling one to reach data densities up to hundreds of gigabits per square inch.[3] Hard disk read/write heads were manufactured first by using the current-in-plane[4] geometry of GMR, and then the current-perpendicular-to-plane[5] GMR heads were implemented, with smaller sensing dimensions and higher output voltages.[6]

Spin valves, as simple GMR devices based on layered ferromagnet/nonmagnet structures, can exhibit hysteretic current-induced magnetization switching[5,7] and high-frequency magnetization precession.[8–13] The latter phenomenon allows transformation of a current input into microwave magnetic oscillations. Due to the rapid reorientation of the magnetic moment of a thin free magnetic layer relative to the pinned magnetic moment of the thick (reference) layer, these oscillations can be observed as oscillations in the GMR value. The magnetic moment of the reference layer is kept constant either by making this layer sufficiently thick or by coupling it to an antiferromagnetic substrate.[4]

Ferromagnetic materials are usually characterized by a preferred magnetization orientation, i.e., the magnetic easy axis, and described by the anisotropy constant K. The free sensing layer of a spin valve is usually made in the form of an elliptic cylinder several nanometers thick, with the major and minor axes making a ratio of at least 2:1 and measuring dozens of nanometers. Due to the demagnetizing field effect, the easy magnetization axis is aligned with the major axis of the ellipsoid. In addition, there is also a planar anisotropy due to the small thickness of the free layer, with the easy magnetization plane coinciding with the film plane and described by the anisotropy constant K_p.

Applying a magnetic field along the easy axis creates the most efficient magnetic torques. This is used in the hard disk read/write heads, where the magnetic signals representing the bits 0 and 1 have opposite magnetization orientations along the easy axis. It was also shown that application of tilted fields affects the magnitudes of switching field and switching time,[14–16] opening new perspectives for information technology. Moreover, the spin valves operating under an arbitrary orientation of the applied magnetic field are successfully used in the automobile industry, offering an accurate way of noncontact angle measurement.[17,18] In contrast to the commonly used anisotropic magnetoresistance sensors working at angles from 0° to 90°, the GMR effect allows one to measure the full revolution (360°).[19]

Theoretical investigations of the current-induced magnetic dynamics in spin valves are mostly based on the Landau–Lifshitz–Gilbert (LLG) equation, in which the spin torque of Slonczewski type is taken into account.[20,21] In the case of relatively large magnets, it is necessary to use micromagnetic simulations, dividing the object into smaller domains (see, e.g., Refs. 22–27). However, in some cases, the dynamics of the free magnetic layer can be described quite well by the macrospin approximation,[28,29] in which the free layer is represented by a monodomain ferromagnet with the magnetization vector $\mathbf{M}$ of constant length M_s defined by the saturation magnetization of the corresponding material. The temporal reorientation of $\mathbf{M}$ follows the LLG equation,[8,30–35] and may be controlled by the external magnetic field and injected spin-polarized current.

The macrospin model allows one to understand the main dynamical modes observed in experiments, in particular, the magnetization reversal, magnetization pinning in canted states[31] (with the magnetization vector making a certain angle with the easy axis), and steady precessional modes roughly in or out of the easy magnetization plane. These oscillation modes have been predicted to be of gigahertz frequencies, which is in good agreement with the experimental

data.[8] Upon transition between the in-plane and out-of-plane precessions, the theory predicts an abrupt frequency jump,[8,29,36,37] which however is not clearly revealed in experimental results (see, e.g., Refs. 10 and 38). However, one should bear in mind the limitations of the macrospin model. First of all, the macrospin model does not apply to multidomain sensing layers. Second, the macrospin model does not allow one to study the internal dynamics of the sensing layer, i.e., nonuniform dynamical states. The latter also means that the role of Ampere's field cannot be properly described in the macrospin model.

In this paper, we present results of our numerical studies of the macrospin dynamics in a general case, i.e., when the magnetic field and spin-current polarization form arbitrary angles with the easy magnetization axis. We find dynamical modes that cannot be attained by exciting the system along its easy magnetization axis. Despite some similarities to the known macrospin oscillations, these dynamical modes have interesting properties that can be useful for applications. Moreover, our approach can explain the frequency jumps observed experimentally.

The paper is organized as follows. In Sec. II, we describe the model, outline the calculation procedure, and explain the main parameters that are required for an efficient characterization of the system. In Sec. III, we investigate the macrospin dynamics for the collinear situation, when both magnetic field and spin-current polarization are parallel to the easy axis. Sections IV and V include the analysis of the system behavior under separate deviations of the magnetic field and current polarization from the easy axis. In Sec. VI, we consider the general case when both magnetic field and current polarization are oriented at arbitrary angles with respect to the magnetic easy axis. Finally, Sec. VII includes the summary and discussion of the results.

II. THEORETICAL MODEL AND CALCULATION DETAILS

Let us consider a magnetic particle whose magnetic moment $\mathbf{M}$ is constant in magnitude, $|\mathbf{M}|=M_s$, while its orientation is described by the spherical angles φ and θ. The particle is assumed to be in the form of a thin-film ellipsoid lying in the yz plane, with the magnetic easy axis oriented along the z axis. Apart from this, the charge current J is assumed to be spin polarized and flowing perpendicularly to the film plane, with the corresponding spin polarization vector $\mathbf{n}$ oriented in the film plane and forming an angle Φ with the z axis. The external magnetic field $\mathbf{H}$ is also applied in the film plane, at an angle Ψ to the magnetic easy axis. We note that the current of magnetic moment associated with the spin current is oriented opposite to the vector $\mathbf{n}$.

Upon normalization of the current and magnetic field, respectively, to $4edSK/\hbar\eta$ and $H_k=2K/M_s$, both quantities can be reduced to the dimensionless variables $\mathbf{h}_s=h_s\mathbf{n}=(J\hbar\eta/4edSK)\mathbf{n}$ and $\mathbf{h}=\mathbf{H}/H_k$. Here, e is the electron charge, d and S are the thickness and area of the free layer, and η represents the current polarization degree ($\eta>0$ by definition). We also recall that according to our definitions, positive h_s means that electrons are injected to the magnetic body through the considered interface. It is also convenient to introduce the longitudinal and transversal (with respect to the easy axis) components $h_{s\parallel}=h_s\cos\Phi$, $h_\parallel=h\cos\Psi$ and $h_{s\perp}=h_s\sin\Phi$, $h_\perp=h\sin\Psi$, respectively.

The total energy density of the magnetic particle can be written in the form

$$U_{\text{total}}(\theta,\varphi)=U_K+U_P-U_H, \tag{1}$$

where

$$U_K=K\sin^2\theta, \quad U_P=K_p(\sin^2\theta\cos^2\varphi-1),$$

$$U_H=2K(h_\perp\sin\theta\sin\varphi+h_\parallel\cos\theta), \tag{2}$$

are the contributions due to uniaxial anisotropy, U_K, easy plane anisotropy, U_P, and Zeeman energy, U_H. When the magnetic field is applied along the magnetic easy axis,[8,28,30] the component $h_\perp$ is equal to zero and the corresponding Zeeman energy term U_H becomes independent of the azimuthal angle φ. Such a collinear situation describes a simplified magnetic energy landscape, $U_{\text{total}}(\theta,\varphi)$, that may exclude a certain set of dynamical modes characteristic of noncollinear situations. Thus, it is important to study the case of $\Psi\neq 0$ and to also consider noncollinear current polarization, $\Phi\neq 0$. The spectrum of possible operation modes of the system may be broader in such a general situation, which, in turn, may lead to new application possibilities.

The Landau–Lifshitz–Gilbert equation with the spin torque included[30] can be transformed into the following set of differential equations for the spherical angles describing the macrospin orientation:[39]

$$\frac{\partial\theta}{\partial\tau}=-\sin\theta(\alpha A-B), \quad \frac{\partial\varphi}{\partial\tau}=\alpha B+A, \tag{3}$$

where

$$A=Z(\varphi)\cos\theta+h_\parallel-(h_\perp\cos\theta\sin\varphi+h_{s\perp}\cos\varphi)/\sin\theta,$$

$$B=\frac{1}{2}h_p\sin 2\varphi+h_{s\parallel}+(h_\perp\cos\varphi-h_{s\perp}\cos\theta\sin\varphi)/\sin\theta,$$

$$Z(\varphi)\equiv(1+h_p\cos^2\varphi), \quad \tau=t/[(1+\alpha^2)/\gamma H_k]. \tag{4}$$

The time scale τ of the system is defined by the damping coefficient α, gyromagnetic ratio $\gamma=2\mu_b/\hbar$, and the anisotropy field H_k. For our calculations, we used the typical parameters for cobalt:[8] $\alpha=0.014$, $K_p=10$ kOe, and $H_k=500$ Oe ($h_p=K_p/K=20$). The applied magnetic field was changed from zero to 15 kOe ($h=0-30$). We note that current-induced switching and magnetic dynamics strongly depend on the damping parameter α. For instance, critical switching current significantly increases with increasing α.

In the stationary case, Eq. (3) has four equilibrium states, including $\mathbf{m}=\{0,0,1\}$ and $\mathbf{m}=\{0,0,-1\}$, with $\mathbf{m}=\mathbf{M}/M_s$. In the following, we assume that the initial orientation of the magnetic moment at time $\tau=0$ is in the vicinity of the equilibrium state $m_z=-1$, setting the corresponding spherical angles to $\theta=0.99\pi$ and $\phi=0$.[28] For the initial orientation of the magnetic moment $\mathbf{m}$ along the $-z$ axis, we will be using the terms "parallel" and "antiparallel" for the resulting mag-

netic moment orientation corresponding to $m_z=-1$ and $m_z=+1$, respectively.

Equation (3) was integrated numerically using the Runge–Kutta method of fourth order, which assures a good solution stability for different integration time steps. We used the integration step $\tau_{\text{int}}=1$ ps and calculated 35 000 points for each $\theta(\tau)$ and $\varphi(\tau)$. Three-dimensional phase portraits of the system were constructed using the components $m_x=\sin\theta\cos\varphi$, $m_y=\sin\theta\sin\varphi$, and $m_z=\cos\theta$, which describe the orientation of the magnetic moment at a given time. Only the last 10 000 points of the resulting phase trajectory were considered, excluding the intermediate transition processes and focusing on the final steady states.

The most convenient form of presenting the data on system evolution with the changes of several external control parameters is to build relevant dynamic diagrams.[8,28,30,41–44] This process can be significantly simplified with a proper choice of the numerical characteristics of the system, allowing unambiguous classification of different oscillation modes. For this purpose, we selected three quantities: amplitude Δm_z, time-averaged value m_z^A, and Hausdorff dimension D_H. Observation of the magnetization component parallel to the easy axis is very important from the application point of view. In particular, its mean value m_z^A averaged over a certain period of time allows one to calculate the magnetoresistance of the spin valve, provided the direction of the magnetic moment in the fixed layer is known. In our case, $\mathbf{h}_s$ describes the spin current which enters the free magnetic layer. In real structures, its magnitude and orientation may be different from those in the fixed magnetic layer (e.g., due to the spin accumulation and spin relaxation in the thin nonmagnetic layer of the spin valve). In general, the expression for normalized magnetoresistivity[45] includes the averaged value of the zenithal angle θ^A or the averaged z component $m_z^A=\cos\theta^A$,

$$r=\frac{1-\cos^2(\theta^A/2)}{1+\cos^2(\theta^A/2)}=\frac{1-m_z^A}{3+m_z^A}. \tag{5}$$

If one is going to perform GMR measurements in order to extract the microwave signal generated by a spin current, it is especially important to have the amplitudes of resistivity oscillations as high as possible (to improve the signal to noise ratio). The scale of such ultrafast resistivity dynamics will correspond to the oscillation amplitude Δm_z. On the other hand, it is worthy to note that m_z-related characteristics do not allow one to distinguish numerically between some particular states of the system. For example, in a canted state, the magnetization vector of the system is fixed at a certain angle with respect to the magnetic easy axis.[31] If—upon changes of the applied field or injected current—this state loses stability, the magnetization vector will start a small-angle precession around the canted axis. The time averaging of such a motion results in values that are practically indistinguishable from m_z^A characterizing the initial canted state. Thus, the transition between states with fixed and precessing moments is detectable by an increase in Δm_z.

As we know, the macrospin approximation predicts two types of steady magnetization precessions, which occur either in or out of the easy magnetization plane.[8,28,46] The characteristic time dependence of the individual magnetization components for these precession types is shown in the left panel of Fig. 1 [out-of-plane precession (OPP), top panel; in-plane precession (IPP), bottom panel]. As one can see, the $m_z(t)$ curves are almost identical in both cases, which yield very similar values of the oscillation amplitude ($\Delta m_z^{(\text{OPP})}=1.318$, $\Delta m_z^{(\text{IPP})}=1.313$) and mean value ($m_z^{A(\text{OPP})}=-0.648$, $m_z^{A(\text{IPP})}=-0.633$). This numerical ambiguity can be effectively solved by calculating a metric dimension[47] of the phase portrait such as the Hausdorff dimension

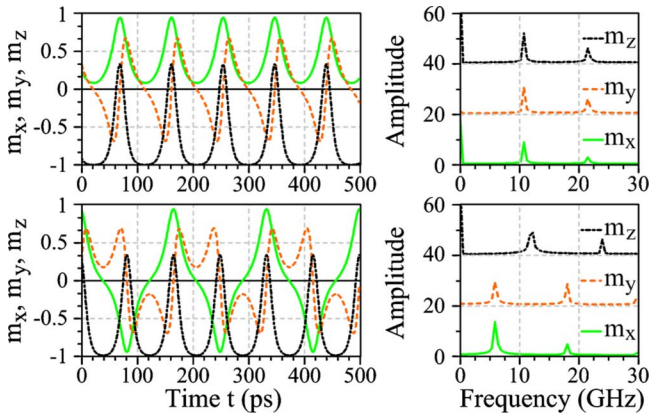

FIG. 1. (Color online) Oscillations of magnetization components and the respective Fourier spectra for steady out-of-plane ($h_s=0.34$, $h=7$; top panels) and in-plane ($h_s=0.31$, $h=7$; bottom panels) precession. The curves for m_x are green, for m_y orange, and for m_z black. Spectral plots are incrementally offset vertically by 20.

$$D_H=-\lim_{\epsilon\to 0}\frac{\log N}{\log \epsilon}, \tag{6}$$

where N is the number of n-dimensional cubes (of side length ϵ), required to cover the phase trajectory. If the system dynamics converges to a single limit cycle characteristic for the out-of-plane precession, its dimension will be $D_H\geq 1$ (the value of unity corresponds to a line, and the value of 2 for a completely covered plane). Upon the addition of another loop forming the phase portrait for the in-plane magnetization precession, the Hausdorff dimension jumps to a higher value (e.g., for the time profiles of magnetization components presented in Fig. 1, one finds $D_H^{(\text{OPP})}=1.28$ and $D_H^{(\text{IPP})}=1.42$, respectively). If for a given set of parameters the macrospin becomes fixed along a certain direction, the corresponding phase portrait will consist of a single point, resulting in $N=1$ and, consequently, $D_H=0$. Therefore, the Hausdorff dimension allows efficient distinction between steady precessional modes, but cannot discern fixed magnetization vector states. In turn, this task can be easily solved using the average m_z^A, which becomes ± 1 for antiparallel and parallel macrospin orientations, respectively, and achieves intermediate values for the canted states. Therefore, the three characteristics, D_H, m_z^A, and Δm_z, form an efficient and mutually complementary set of parameters, which allow easy numerical classification of different magnetic states and

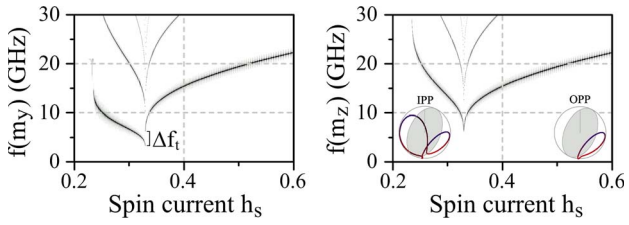

FIG. 2. (Color online) Frequency for the m_y and m_z components as a function of spin current for $h=7$; the peak positions are shown as black curves. Frequency doubling jump Δf_t upon transition between the out-of-plane and in-plane oscillations is seen in the m_y spectra, but is absent for m_z.

can be successfully used for the construction of the system phase diagram.

Another important parameter for spintronic devices is the gigahertz-order frequency of the generated microwave oscillations.[8] As one can see from the Fourier spectra presented in Fig. 1, all the peaks for the out-of-plane precession are aligned at the same frequency $f \approx 11.3$ GHz, while for the in-plane precession only the fundamental m_z peak is at 11.5 GHz whereas those for m_x and m_y are located at half-frequency $f \approx 5.75$ GHz. This feature has a simple explanation: The IPP modes have two loops symmetric with respect to the easy plane, which requires twice the time for the phase point to encircle the trajectory in the xy plane, which in turn yields a twice lower oscillation frequency. With regard to the projection on the z axis, both loops coincide, so the oscillation period remains the same as that for a single-loop OPP limit cycle. This question was partly discussed by Xiao *et al.*,[28] who showed that the magnetic field dependence of the macrospin in-plane precession frequency can be successfully described by the doubled value of the Kittel frequency. Therefore, if we calculate the overall magnetization precession frequency (see, e.g., Refs. 8, 29, and 37), it reveals a characteristic two-times frequency increase upon the OPP or IPP transition. However, if the precession frequency is measured via GMR effect, it will be essentially determined by the behavior of m_z and will not reveal the frequency jump (e.g., the measurement data presented in Ref. 10).

The characteristic current dependence of the Fourier spectra on the collinear situation is shown in Fig. 2 separately for m_y and m_z components. As anticipated, the minor harmonics follow the behavior of the fundamental ones, also revealing a jump for m_y and being continuous for m_z. Therefore, in the following discussion, we will mention only the changes in the behavior of the fundamental harmonics. If performance of an extensive modeling of macrospin dynamics encompassing different phase states of the system is required, the overall calculation time can be significantly reduced, omitting the calculations of phase variable spectra when steady magnetization precession is absent. Such regions can be determined by nonzero values of less calculation-expensive quantities, such as the oscillation amplitude Δm_z or Hausdorff dimension D_H.

III. COLLINEAR SITUATION

First, we consider the evolution of the system upon variation of h_s at fixed h. The typical situation is illustrated in Fig. 3 for $h=7$. For $h_s \leq 0.228$, the magnetic moment remains in the upper state $m_z=+1$. Upon an increase in h_s, the upper equilibrium state loses its stability and the phase point becomes attracted to the limit cycle with oscillation frequencies overcoming 20 GHz at signal amplitudes $\Delta m_z > 1$. Under larger h_s, the limit cycle consists of two symmetric loops [Fig. 3(a)]. Considering the system over a large time scale and averaging the magnetization components, one gets $m_x^A \to 0$ as if the magnetization dynamics would take place in the easy magnetization plane only. Because of this, we will refer to this type of motion as the in-plane precession, even for significant amplitudes of m_x.

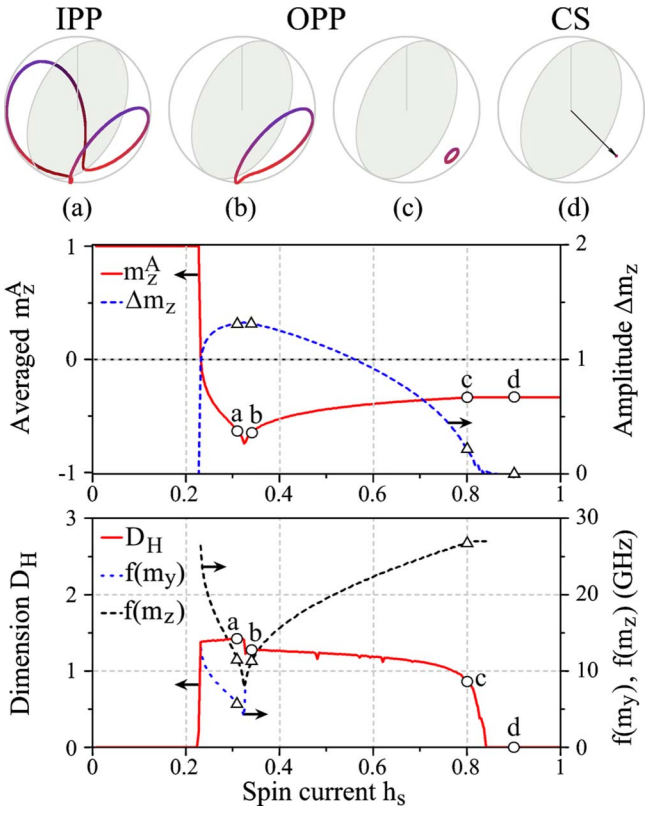

FIG. 3. (Color online) Evolution of the magnetic moment with the changes of the spin current under the constant magnetic field $h=7$. Plots show the average magnetization m_z^A, magnetization amplitude Δm_z (top panel) and Hausdorff dimension D_H and oscillation frequencies $f(m_y)$ and $f(m_z)$ (bottom panel). Most characteristic phase portraits are shown above for (a) in-plane precession ($h_s=0.31$), (b) out-of-plane magnetization precession ($h_s=0.34$), (c) small-amplitude limit cycle nucleated from the canted state ($h_s=0.8$), and (d) canted state for $h_s=0.9$. For three-dimensional phase portraits, the unit sphere, easy magnetization plane yz, and positive segment of easy axis z are plotted as guides for the eye.

Upon reaching $h_s \approx 0.325$, the system undergoes a period halving bifurcation, forming a single out-of-plane precession limit cycle [Fig. 3(b)]. Depending on the values of h and h_s, the OPP cycle may be situated either to the left or to the right of the easy magnetization plane, leading to different signs of the m_x component. As one can see from Fig. 3, neither m_z^A nor Δm_z allows one to distinguish between the IPP and OPP modes numerically. On the contrary, the Hausdorff dimension curve features two distinct plateaus for each oscillation

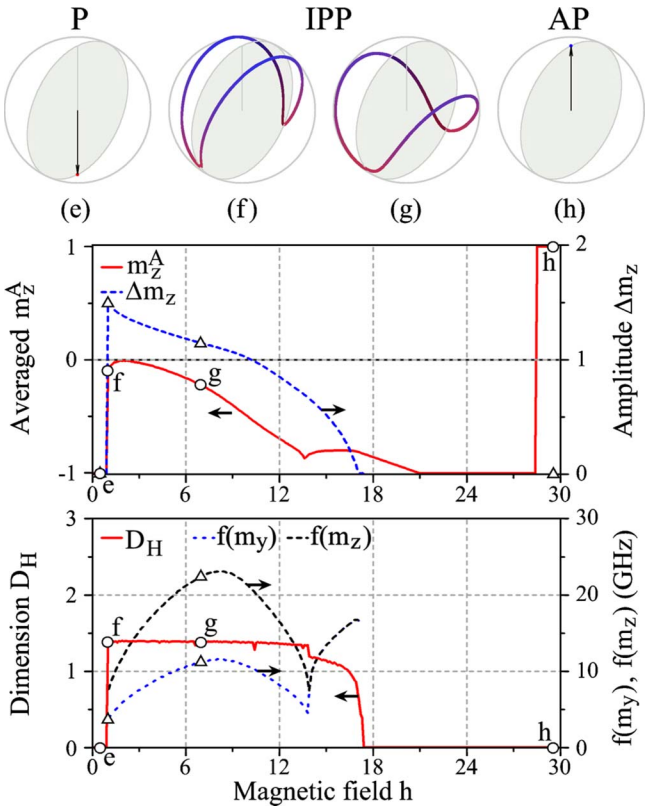

FIG. 4. (Color online) Evolution of magnetic dynamics with increasing magnetic field under the constant spin current h_s=0.235: average m_z^A and amplitude Δm_z of m_z component (top panel) and Hausdorff dimension D_H and oscillation frequencies $f(m_y)$ and $f(m_z)$ (bottom panel). Most characteristic phase portraits are presented above for (e) parallel alignment of magnetic moment with regards to spin-current polarization **n** (h=0.5), (f) narrow in-plane precession (h=1), (g) in-plane precession (h=7), and (h) magnetization reversal to antiparallel state (h=29.5).

mode (Fig. 3). The largest amplitude Δm_z can be observed at the OPP/IPP transition point, but the corresponding GMR-detectable frequency $f(m_z)$ is only 8.2 GHz, the lowest in the considered range of h_s.

For larger incident currents, the amplitude of the OPP cycle becomes smaller [Fig. 3(c)], precluding possibilities to use the increasing magnetization precession frequencies up to $f(m_y)=f(m_z)\approx 27$ GHz. Upon approaching $h_s\approx 0.82$, the system undergoes a reverse Hopf bifurcation,[47] causing the small-amplitude out-of-plane precession limit cycle to converge into a canted state [Fig. 3(d)] with $m_z\equiv m_z^A=-0.33$. The latter magnetization component coincides with the value 1/3 obtained from the equation $m_z=-h/(h_p+1)$ for the stationary solutions (see Ref. 40). As discussed above, the phase transition between OPP and canted state (CS) can be detected by nonzero values of the amplitude Δm_z and dimension D_H.

Evolution of the system upon varying the magnetic field at a fixed value of spin current is shown in Fig. 4. As one can see from Fig. 4, for $h<1$ the system remains in the parallel state [Fig. 4(e)]. Under a larger field, the macrospin switches to the in-plane precession, with the maximum amplitude of the m_z component equal to 1.5 at h=1 [Fig. 4(f)]. Increasing

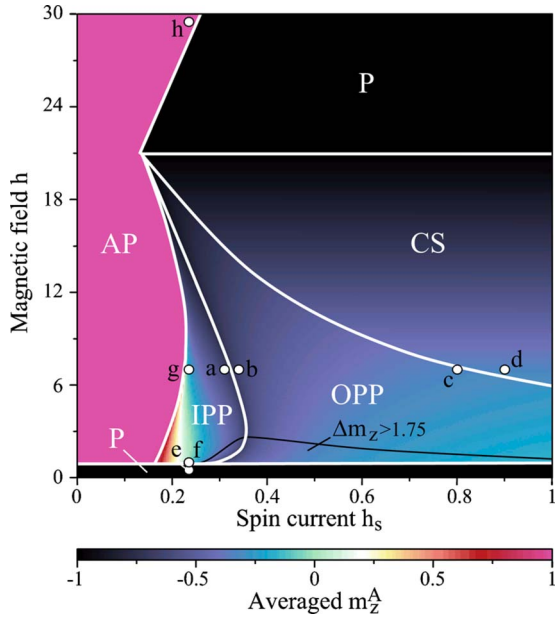

FIG. 5. (Color online) Dynamic state diagram for collinear (Ψ=0, Φ=0) situation: parallel (P) and antiparallel (AP) states, canted states (CS), and in-plane (IPP) and out-of-plane (OPP) steady magnetization precession. Colors represent m_z^A as a function of incident spin current h_s and applied magnetic field h. Boundaries between different states were built using also $D_H(h_s,h)$ and $\Delta m_z(h_s,h)$. Thin black curve limits the region where magnetization oscillations are characterized with a large amplitude $\Delta m_z>1.75$. The letters a–h correspond to the phase portraits shown in Figs. 3 and 4.

h increases the angle between the branches of the limit cycle [Fig. 4(g)], decreasing both Δm_z and m_z^A in a nonlinear way. It is important to emphasize that the oscillation frequency of the in-plane precessional states has a pronounced maximum $f(m_z)$=23.1 GHz at h=8.3, with a considerable signal amplitude Δm_z=1.1. A further increase in the applied field leads to IPP/OPP bifurcation at $h\approx 13.8$, which is clearly distinguishable from the D_H, m_z^A, and frequency curves. The limit cycle shrinks under stronger fields [Fig. 4, $\Delta m_z(h)$ curve] and, after reverse Hopf bifurcation at h=17, turns into a focus corresponding to a canted state. Further, $m_z^A(h)$ dynamics follows a linear dependence, characteristic of the stationary solutions of Eq. (3), and for $21<h<28.4$, the magnetic moment becomes locked in the parallel state. Upon overcoming the latter value, a magnetization reversal takes place and the macrospin converges to the antiparallel state $m_z=+1$ [Fig. 4(h)].

Using the methodology described above, it is possible to construct the dynamical phase diagram with respect to both applied magnetic field h and injected spin current h_s, with well defined boundaries between the phase states of the system (Fig. 5). To simplify a comparison with the dynamics discussed above (Figs. 3 and 4), the corresponding $[h_s,h]$ points are marked on the diagram.

For the collinear situation, several phase boundaries can be found analytically, namely:

(1) The lower and upper field limits of the magnetization

precession states correspond to the values bounding the regions describing the existence of equilibrium solutions of the system (3) (Refs. 31 and 40):

$$h_{\text{low}} = 1, \quad h_{\text{high}} = 1 + h_p; \tag{7}$$

(2) The boundary between the canted states (stable focus) and the out-of plane precession cycle (nucleated from an unstable focus) obeys the neutral stability condition:[31,40]

$$h_b = -\xi + \sqrt{\xi^2 + (1 + h_p/2 + \sqrt{\varpi})^2 - \varpi/4}, \tag{8}$$

with $\xi = h_s/\alpha$ and $\varpi = h_p^2 - 4h_s^2$. Expression (8) can be derived from the characteristic equation obtained for the case when small perturbations are applied to the equilibrium solutions of the system;[40]

(3) The switching boundary between the in-plane precession and antiparallel states for $h \leq 1$ is described by the low-field switching threshold obtained for small-angle magnetization precession by setting the average variation of the system energy to zero:[30]

$$h_{\text{LF}} = h_s/\alpha - (1 + h_p/2); \tag{9}$$

(4) The magnetization switching between parallel and antiparallel states for $h > h_p + 1$ agrees well with the high-field switching threshold formula corresponding to the maximum of the average system energy variation:[30]

$$h_{\text{HF}} = |h_s|/\alpha + 1 + h_p/2; \tag{10}$$

(5) The linear portion of the boundary between the in-plane and out-of-plane precession modes for $1 \ll h < h_p + 1$, mirror-symmetric to the h_{HF} line regarding $h = h_p + 1$, can be fitted with the similar expression

$$h_{\text{OPP/IPP}} = -h_s/\alpha + 1 + 3h_p/2. \tag{11}$$

The phase diagram for the collinear situation (Fig. 5) allows one to define several ranges of parameter values that lead to the most interesting and promising applications. The largest changes of the average component m_z^A can be achieved upon parallel (P)/antiparallel (AP) magnetization reversal at low field ($h = 1$, $h_s < 0.168$) or high field ($h > h_p + 1 = 21$ and h_s satisfying Eq. (10). Steady magnetization precession exists in a wedge-shaped area with the boundaries described by Eqs. (7)–(9). The largest oscillation amplitude Δm_z is achievable for the lowest applied field values $h \geq 1$ (Fig. 5; area below thin black curve denotes $\Delta m_z > 1.75$). These high-amplitude phase states are characterized by oscillation frequencies below 10 GHz and include mostly out-of-plane precession modes. Oscillation frequencies overcoming 20 GHz can be achieved in the vicinity of the IPP/AP transition boundary. To obtain GMR data with high signal to noise ratio, one should choose h and h_s close to the maximum of the IPP/AP boundary as a function of applied magnetic field (i.e., $7 \lesssim h \lesssim 11$ and $h_s \gtrsim 0.235$). Under lower magnetic fields, switching to the antiparallel state prevails in the macrospin dynamics, making the oscillation amplitudes Δm_z at the IPP/AP boundary smaller; this fact is also illustrated by the high values of the average magnetization component $m_z^A \gtrsim 0.7$ (Fig. 5).

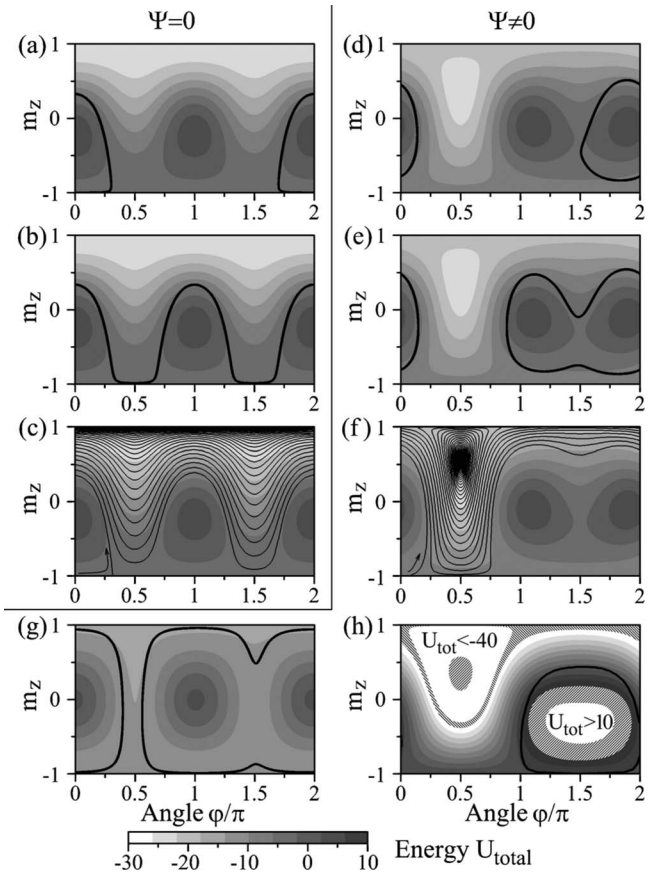

FIG. 6. Magnetic energy landscape (plotted in the coordinates $m_z = \cos\theta$, φ) and phase trajectories of macrospin magnetization. Collinear situation ($\Psi = 0$) and $h = 7$: (a) $h_s = 0.34$, out-of-plane precession; (b) $h_s = 0.31$, in-plane precession; and (c) $h_s = 0$, magnetization reversal from the initial state $[\theta = 0.99\pi, \varphi = 0]$ to $m_z = +1$. Noncollinear situation ($\Psi = \pi/3$) and $h = 7$: (d) $h_s = 0.6$, out-of-plane-precession; (e) $h_s = 0.7$, in-plane precession; and (f) $h_s = 0$, magnetization reversal to the tilted antiparallel state with $\theta = \pi/3 \Rightarrow m_z = +1/2$. Also for $h_s = 0.7$: (g) $h = 0.6$, narrow in-plane precession with the amplitude $\Delta m_z \to 2$; and (h) $h = 24.4$, wide-angle precession cycle encompassing both energy maxima.

IV. EFFECT OF NONCOLLINEAR MAGNETIC FIELD ON MACROSPIN DYNAMICS

The application of a magnetic field in the film plane at an angle Ψ to the easy magnetization axis introduces the azimuthal-angle dependence of the Zeeman energy (2), which influences the energy landscape of the system. The most illustrative cases of the total energy distribution, calculated according to Eq. (1), and the corresponding phase trajectories are presented in Fig. 6. The plots are given in the coordinates $[\varphi/\pi, m_z]$ rather than in $[\varphi, \theta]$ (see, e.g., Ref. 48); such a presentation facilitates comparison with the three-dimensional plots of the phase portraits. As one can see from this figure, for the collinear situation [Figs. 6(a)–6(c)] with an applied magnetic field, the plots feature the lowest energy value for the upper pole $m_z = +1$. Without a magnetic field, the maxima of $U_{\text{total}}(\theta, \varphi)$, determined by the easy plane anisotropy term U_P, are located at $\theta = \pi/2$ and $\varphi = 0, \pi$. The nonzero Zeeman energy shifts them toward

$m_z=-1$. Under spin-current injection, the magnetic moment can be switched to the steady precession modes (OPP or IPP), causing the phase point to encompass, respectively, one or two energy maxima [Figs. 6(a) and 6(b)]. When h_s is smaller than the threshold required to trigger precession, P/AP switching can occur. As the bottom pole where $m_z=-1$ is unstable, the phase point leaves it and coils away[49] to the upper pole following the energy gradient [Fig. 6(c)].

Tilting the magnetic field causes the rotation of the energy pattern around the x axis, which tries to align its minimum with the magnetic field orientation. For further discussion, we have chosen the particular case of $\Psi=\pi/3$, for which the upper pole will be moved to $m_z=\cos\Psi=1/2$. As a result, the energy maxima approach each other along the φ axis, leading to the formation of a low energy "valley," defining the preferred path for the magnetization switching [Fig. 6(f); cf. Fig. 6(c) calculated for the same h and h_s].

A tilted magnetic field leads to a rotation of the magnetization vector trajectory to adjust it to the energy landscape. This effect is clearly seen by a comparison of the OPP and IPP cycles for the cases of $\Psi=0$ and $\Psi=\pi/3$ [Figs. 6(a) and 6(d) and Figs. 6(b) and 6(e), respectively]. The most important consequence of such a rotation is the remapping of the magnetization components according to

$$m_y' = m_y \cos\Psi - m_z \sin\Psi,$$

$$m_z' = m_y \sin\Psi + m_z \cos\Psi. \tag{12}$$

As we have seen before (Fig. 1, bottom panel), the IPP cycles are usually characterized by high Δm_y amplitudes that may be close to 2, while the useful Δm_z amplitude in the collinear situation is limited by ≈ 1.5. In the noncollinear case with large angles Ψ, the component m_y is practically remapped to m_z, leading to high-amplitude magnetization oscillations along the easy axis. A characteristic example of such oscillations with $\Delta m_z \to 2$ is presented in Fig. 6(g) (energy landscape and magnetization trajectory) and on the top panel of Fig. 7 (magnetization components and their Fourier spectra). Comparing the latter to the spectra for the nontilted IPP cycle (Fig. 1, bottom panel), effective swapping of m_y and m_z oscillations can be easily noticed. Therefore, contrary to the collinear situation, for $\Psi \approx 1$ one observes a twofold increase in the m_y oscillation frequency upon transition between the in- and out-of-plane precessions, and the m_z frequency does not feature this discontinuity.

Another very important application-related case can be achieved for high applied fields, when the distance between energy maxima becomes small and the phase trajectory can encompass both of them in one wide angle precession (WAP) loop [Fig. 6(h)]. Individual magnetization components and the corresponding Fourier spectra for this phase portrait are shown in Fig. 7 (bottom panel). The presence of weak secondary peaks on $f(m_y)$ curves indicates that the given magnetic motion represents in-plane precession, characterized with the frequencies overcoming 30 GHz at large amplitudes $\Delta m_z \approx 1.5$.

The main characteristics of the system for $h=7$, $\Psi=\pi/3$, and varying h_s are displayed in Fig. 8. As one can see for $h_s \lesssim 0.4$, the magnetic moment switches to the orientation

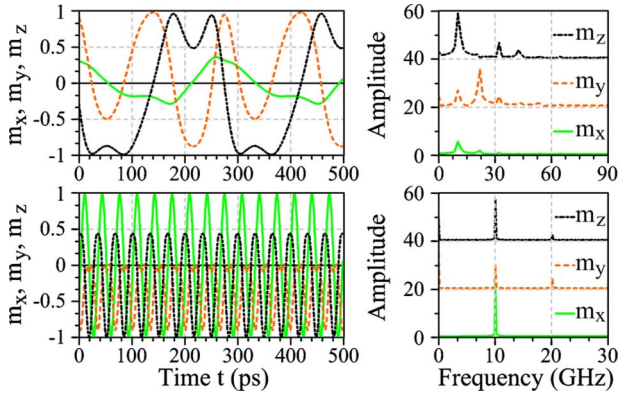

FIG. 7. (Color online) Oscillation of individual magnetization components and corresponding Fourier spectra for m_x (orange), m_y (green), and m_z (black) for the case of noncollinear LLG ($\Psi=\pi/3$). Spectral curves are incrementally offset vertically by 20 to improve the presentation. Top panels illustrate narrow in-plane precession for $h=0.6$, $h_s=0.7$; bottom panels present the data for wide angle precession cycle ($h=24.4$, $h_s=0.7$).

almost exactly along the direction of the applied magnetic field [Fig. 8(a)]. Since the latter does not form a straight angle with the z axis, we will use the term "tilted antiparallel" (TAP) for this state. Upon an increase in the spin current, the system is characterized by in-plane precession, the amplitude of which has clearly pronounced maxima at $h_s \approx 0.465$ [Fig. 8(b)]. Before this limit, both m_y and m_z frequencies coincide; just after $h_s \approx 0.465$, spectral peaks of the fundamental and second-order harmonics of the m_y component become equal in height [Fig. 8, boxed area on $f(m_y)$ curve]. A further increase in the current decreases both the amplitude and frequency of the precession [Fig. 8(c)]. After period-halving bifurcation at $h_s \approx 0.7$ the macrospin switches to out-of-plane oscillations, which remain present with a considerable amplitude $\Delta m_z \approx 1$ even for $h_s=1$ [Fig. 8(d)]. Upon tilting the magnetic field direction, the initial point $m_z=-1$ for different combinations of h and h_s belongs alternatively to the attraction basin of right and left canted states, determining the position of the out-of-plane precession cycle with regard to the easy plane. As follows from the numerical calculations, these limit cycles are characterized by slightly different amplitudes and oscillation frequencies, forming characteristic steps on the corresponding curves (Fig. 8). For example, the OPP limit cycle illustrated in Fig. 9(f) is similar to that shown in Fig. 8(d), but is situated on the other side of the easy magnetization plane.

Characteristic behavior of the system for the case of fixed $h_s=0.7$ and variable h is illustrated in Fig. 9. As one can see from Fig. 9(e), at $h=1$ the system can support extra large oscillation amplitudes $\Delta m_z \to 2$, which may be very important for practical applications. Upon increasing the magnetic field, one can observe the peak of oscillation frequencies $f(m_z)$ and $f(m_y)$, with the latter reaching 14 GHz. At higher magnetic fields, the system switches to the out-of-plane precession of high frequencies approaching 20 GHz at larger amplitudes Δm_z, contrary to the collinear situation. After that, a bistable range of out-of-plane precession [Fig. 9(f)] follows with characteristic two-level jumps of oscillation fre-

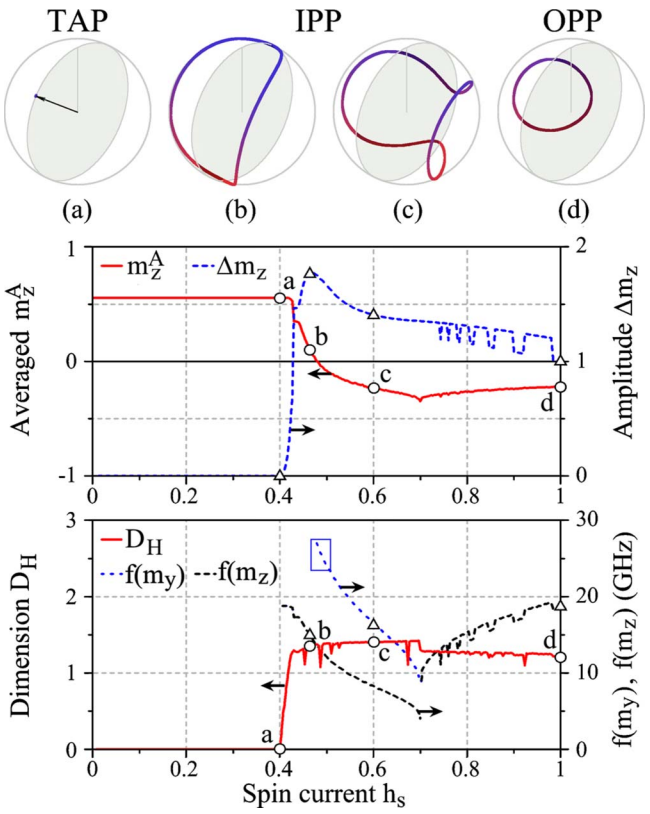

FIG. 8. (Color online) Behavior of noncollinear ($\Psi=\pi/3$) model upon changing h_s for $h=7$: averaged m_z^A and amplitude Δm_z (top panel) and Hausdorff dimension D_H and fundamental oscillation frequencies $f(m_y)$, $f(m_z)$ (bottom panel). Most characteristic phase portraits: (a) $h_s=0.4$, tilted antiparallel state; (b) $h_s=0.465$, modified IPP cycle for magnetization precession around the tilted axis; (c) $h_s=0.6$, in-plane precession; and (d) $h_s=1$, out-of-plane precession cycle. The boxed part of $f(m_y)$ curve is characterized by almost equal spectral peaks for the fundamental and second-order oscillation harmonics.

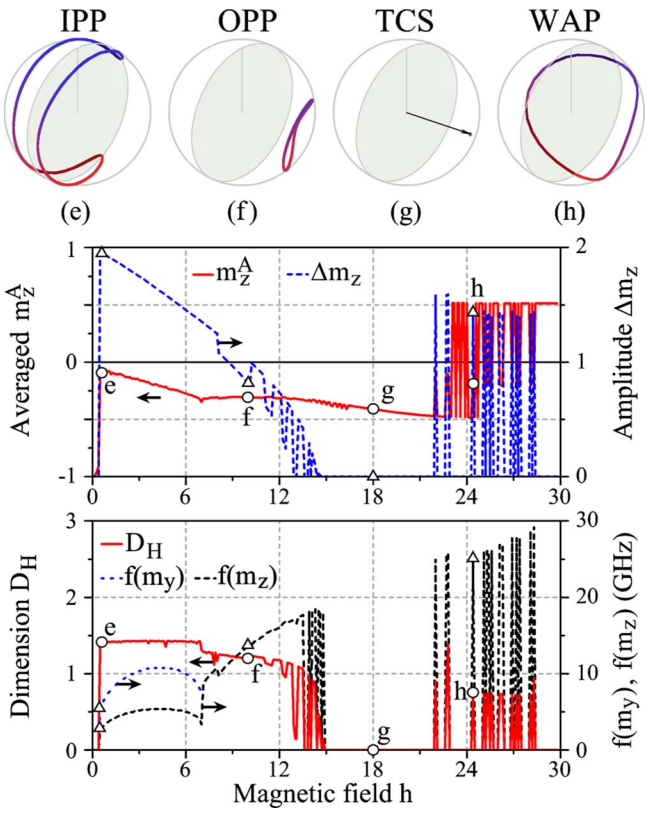

FIG. 9. (Color online) Noncollinear ($\Psi=\pi/3$) model under varying h and constant $h_s=0.7$: averaged m_z^A and amplitude Δm_z (top panel) and dimension D_H and oscillation frequencies $f(m_y)$, $f(m_z)$ (bottom panel). Most characteristic phase portraits are shown for (e) $h=0.6$, narrow in-plane precession with $\Delta m_z \to 2$; (f) $h=10$, out-of plane precession; (g) $h=18$, tilted canted state; and (h) $h=24.4$, wide-angle magnetization precession.

quency and amplitude Δm_z. A further increase in the magnetic field turns the system to the tilted canted states (TCS) [Fig. 9(g)], followed by magnetization reversal to the tilted antiparallel states. The wide-angle precession discussed above [Fig. 9(h)] can be achieved for a certain field range at the boundary between TCS and TAP. The oscillation frequency describing the m_z component of WAP increases with applied field, but the ranges of h allowing achievement of this precession type get narrower.

The dynamic diagram for a noncollinear situation, calculated for $\Psi=\pi/3$ as a function of h_s and h, is shown in Fig. 10. One of the most important details from the figure is the more than twice smaller lower field threshold, allowing one to reach the steady magnetization precession and magnetization reversal already at $h=0.45$ for $\Psi=\pi/3$. Smaller values of $h_\parallel$ result in widening of the boundaries, where the tilted antiparallel states exist, and allow steady precession dynamics for larger values of the injected spin current. One of the most important features achievable in this case is a significant expansion of the IPP region. The thin black curve in the figure encompasses the area where the amplitude Δm_z overcomes 1.75.

A comparison of Fig. 10 with Fig. 5 reveals extensive broadening of the large-amplitude area, which now mainly includes the IPP states. This result may be important from the application point of view, because a wide allowed range of control of parameter values makes it possible to avoid precise parameter tuning to get the desired mode for device operation. As one can see from Fig. 10, wide-angle precession islands represent the series of roughly uniformly spaced bands parallel to the h_s axis, which become blurred for larger h. Such a behavior suggests that this precession could be triggered by a certain discrete set of h values. To reveal the physics behind this phenomenon, additional investigations are required.

It is also worth mentioning that modification of the magnetic energy landscape causes m_z^A to vary with applied field for the tilted antiparallel states (Fig. 10, bottom panel). This effect can be explained by the angular dependence of the equilibrium state of the system, obeying the equation

$$\sin 2\theta^{\mathrm{EQ}} + 2h \sin(\theta^{\mathrm{EQ}} - \Psi) = 0, \tag{13}$$

which can be easily solved numerically; the resulting $\cos \theta^{\mathrm{EQ}}(h)$ agrees well with $m_z^A(h)$ dependence (Fig. 10, bottom panel).

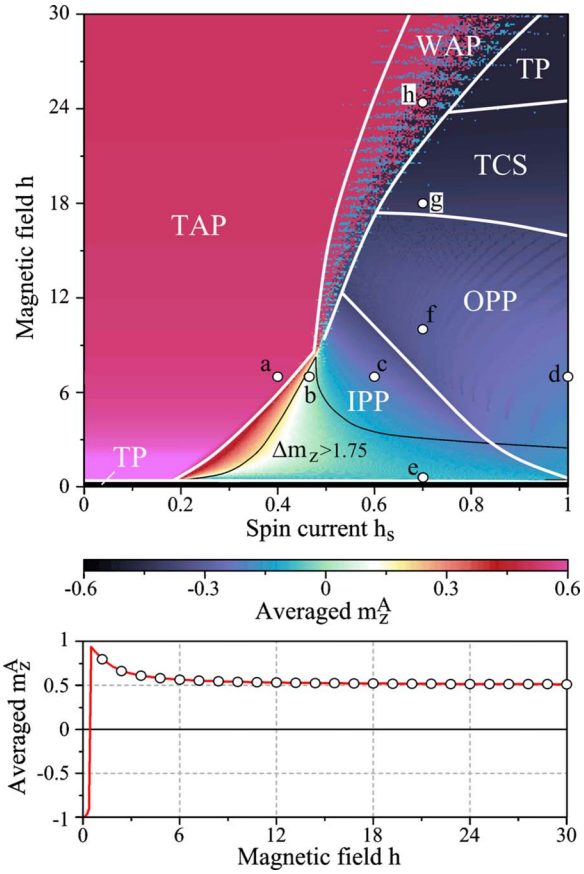

FIG. 10. (Color online) Dynamic state diagram for noncollinear ($\Psi=\pi/3$) situation: parallel (P) and tilted antiparallel (TAP) states, tilted canted states (TCS), steady in- and out-of-plane precession (IPP and OPP). Wide-angle precession (WAP) can be triggered in the set of narrow horizontal regions at TP/TAP boundary. Colors represent the behavior of $m_z^A(h_s,h)$. Boundaries between different system states were reconstructed also considering $D_H(h_s,h)$ and $\Delta m_z(h_s,h)$. Thin black curve encircles the region of large-amplitude oscillations ($\Delta m_z > 1.75$). The letters a–h correspond to the phase portraits shown in Figs. 8 and 9. Bottom panel presents the field dependence of m_z^A for tilted antiparallel states under $h_s=0$ (solid curve) and cos θ^{EQ} (circles).

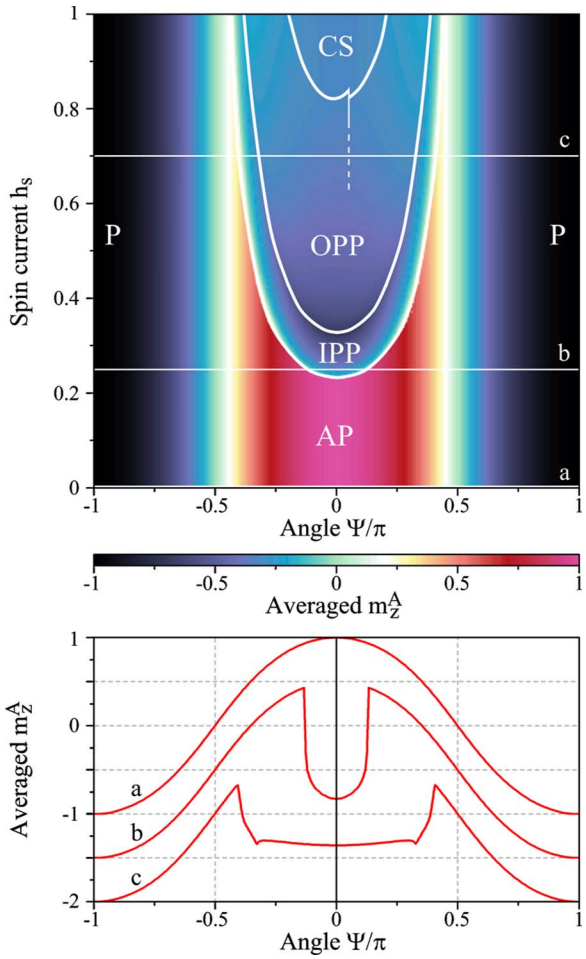

FIG. 11. (Color online) Macrospin state diagram obtained for the constant $h=7$ and variable h_s and Ψ, showing $m_z^A(\Psi,h_s)$ (top panel). White dashed line shows the boundary at either part of which the system converges to the left or right canted state or OPP cycle, respectively. Characteristic dependence of m_z^A for (a) $h_s=0$, (b) $h_s=0.25$, and (c) $h_s=0.7$ (bottom panel). Curves are incrementally offset vertically by 0.5.

Figure 11 presents the dependence of the averaged magnetization m_z^A on noncollinearity angle Ψ and spin current h_s for fixed $h=7$. The boundary between antiparallel and precessional states has a minimum at $h_s=0.23$ for the collinear case ($\Psi=0$). For higher spin currents, steady magnetization precession can be obtained for larger angles; i.e., for $h_s=1$, the OPP limit cycle can be achieved at the maximal angle $\Psi=\pm 1.37=78.5°$. For larger noncollinearity angles, the macrospin is restricted to the ground state, with the magnetization vector pointing along the applied magnetic field.

The most characteristic profiles of $m_z^A(\Psi)$ for $h=7$ and $h_s=0$, 0.25, and 0.7 are shown in the lower panel of Fig. 11. The continuous dependence of $m_z^A(\Psi)$, usually used for angle-measuring sensors,[17,19] can be seen for the low spin currents [Fig. 11(a)]. For values of h_s enabling the in-plane-precession, the $m_z^A(\Psi)$ curve features an abrupt switching to a smooth minimum for small $|\Psi|$ [see Fig. 11(b)]. A further increase in the spin current leads to the appearance of out-of-plane precession modes, for which the average magnetization, and consequently the magnetoresistance of the system, display a wide plateau symmetric with regard to $\Psi=0$ [Fig. 11(c)], confirmed experimentally by Urazhdin *et al.* in Ref. 50. Therefore, in addition to the common angular dependence of magnetoresistance, it is also possible to obtain a constant resistivity response in certain ranges of Ψ, adjustable by the injected current value. This property may simplify the construction of sensors required to allow a fixed magnetization misalignment.

The characteristic plot of angular and field dependence of the average magnetization m_z^A is presented in Fig. 12 for $h_s=0.7$. As one can see from the figure, steady magnetization precession can be obtained at angles up to $\Psi=\pi/2$ at $h\approx 0.95$; for higher field values, the corresponding range of noncollinearity allowing steady precession is narrower. The most interesting profiles $m_z^A(\Psi)$ are presented in the bottom panel of Fig. 12. In particular, for $h=0.35$ [Fig. 12(a)], the angular dependence of the averaged magnetization is characterized by two roughly square-shaped maxima centered at

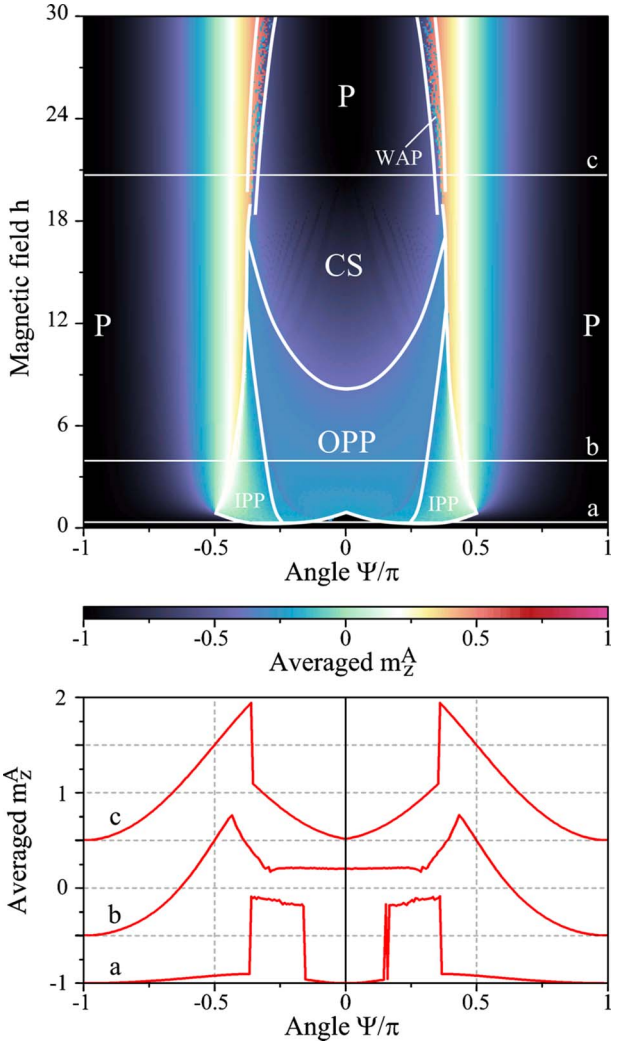

FIG. 12. (Color online) Diagram of macrospin states for different magnetic fields h and angles Ψ between magnetic field and easy magnetization axis z, constructed on the basis of $m_z^A(\Psi,h)$ (top panel) and fixed h_s=0.7. Characteristic angular dependence of the averaged m_z component for (a) h=0.35, (b) h=3.95, and (c) h=20.65 (bottom panel); curves b and c are offset vertically by 0.5 and 1.5, respectively.

$\Psi \approx \pm \pi/4$, beyond which m_z^A tends to −1. As these plateaus correspond to precessional states, they would also be clearly detectable in the frequency domain. With an increase in the magnetic field [Fig. 12(b)], one can observe a wide plateau on the $m_z^A(\Psi)$ curve caused by out-of-plane oscillations, which transforms into a smooth minimum upon transition to the canted states [Fig. 12(c)].

Therefore, noncollinearity of the magnetic field enables a wide number of additional oscillation modes characterized by such properties as high GMR-measurable magnetization precession amplitudes and frequencies. The angular dependence of m_z^A and, consequently, the magnetoresistance of a spintronic device are predicted to show several different selective behaviors that may facilitate implementation of magnetic field sensors with specific characteristics.

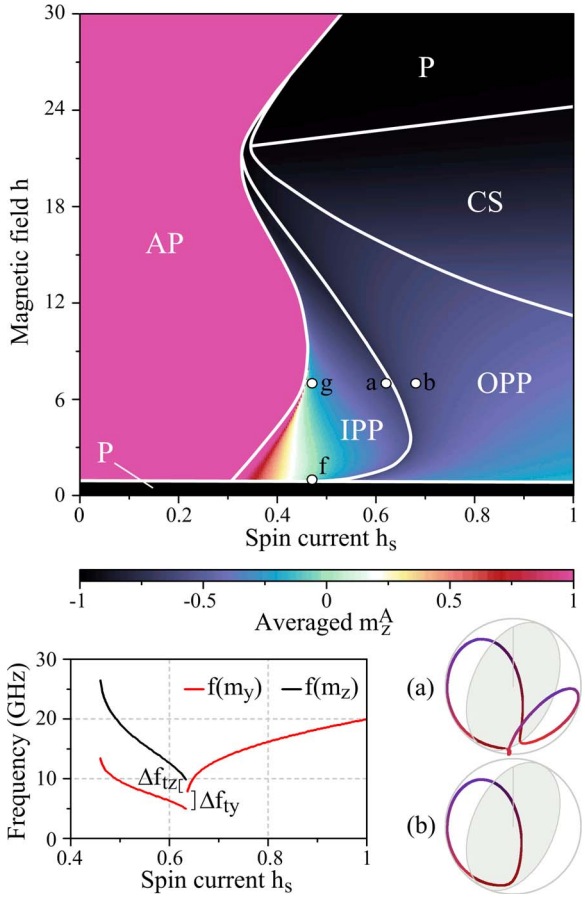

FIG. 13. (Color online) Dynamic state diagram for noncollinear ($\Phi=\pi/3$) model: P and AP states, CS, IPP, and OPP. Characteristic phase portraits (a) h_s=0.62, h=7; (b) h_s=0.68, h=7; (f) h_s=0.47, h=1; and (g) h_s=0.47, h=7 correspond to those shown in Figs. 3 and 4; the only difference consists of side swapping of OPP (b). The lower panel shows fundamental oscillation frequencies for m_y and m_z as a function of applied spin current h_s, featuring discontinuities Δf_{ty} and Δf_{tz} at the OPP/IPP transition point.

V. SPIN CURRENT APPLIED AT AN ANGLE TO THE EASY AXIS

As the angular dependence of the injected spin current does not change the total magnetic energy of the system, variation of the angle Φ between the current polarization vector and easy magnetization axis changes the effective current component $h_{s\|}$, modifying the magnitude of the current torque. To simplify the comparison, we have considered the particular case of $\Phi=\pi/3$, when $h_{s\|}$ is two times smaller than that for the collinear situation. The dynamic state diagram in h and h_s coordinates is presented in Fig. 13. The points a, b, g, and f are plotted at the coordinates $[2h_s,h]$, similar to those shown in Fig. 5. As one can see, all points map into the equivalent regions of the OPP/IPP states. The illustrated phase portraits for h_s=0.62 and h_s=0.68 [Figs. 13(a) and 13(b), respectively] are equal to those considered in the collinear case for h_s=0.31 and h_s=0.34 [Figs. 3(a) and 3(b)], with the only difference that the out-of-plane precession cycle is situated at another side of the easy plane. It is important to emphasize that more significant dissimilarities be-

tween the current-collinear and noncollinear cases exist in the oscillation frequency domain. The characteristic oscillation frequency dependence for the m_y and m_z components on the injected current value is shown in the bottom panel of Fig. 13, revealing the jumps Δf_{ty} and Δf_{tz} for both spectra at the transition point between OPP/IPP modes.

It is remarkable that Eqs. (7)–(11) describing the phase boundaries for macrospin states are generally valid for the case of $\Phi \neq 0$ considered, proving a much smaller influence of the spin-current polarization applied at an angle to the easy axis in comparison to the significant changes rendered to the system by a noncollinear magnetic field. In particular, the lower field allowing steady precessional states remains equal to unity, though a high-field value is not constant anymore and features a linear dependence on h_s. Low- and high-field switching thresholds for the linear boundary between IPP/AP and P/AP states obey the equation similar to Eqs. (9) and (10), generalized for the arbitrary Φ as

$$h_{\mathrm{LF}}^{\Phi} = h_{s\|}/\alpha - (1 + h_p/2), \tag{14}$$

$$h_{\mathrm{HF}}^{\Phi} = |h_{s\|}|/\alpha + 1 + h_p/2. \tag{15}$$

Boundaries between CS/OPP and OPP/IPP states given by Eqs. (8) and (11) do not allow a similar generalization, but the curved slopes calculated using these equations with $h_s \rightarrow h_{s\perp}$ are similar to those shown in Fig. 13.

Figure 14 presents the phase state diagram for the varying noncollinearity angle Φ and spin current h_s, calculated at constant $h=7$. As one can see, the boundary for the precessional and canted states remains practically the same as that shown in Fig. 11 for a noncollinear magnetic field. The essential difference is that beyond the steady precession region, the system relaxes to the antiparallel state with $m_z=+1$. Due to the changes of stability of the stationary solutions of Eqs. (3) for different $h_{s\|}$ and $h_{s\perp}$, the out-of-plane precession cycle and canted state can be situated either to the left or to the right of the easy magnetization plane; the corresponding regions are delimited with a thin white curve in the top panel of Fig. 14. The bottom panel of Fig. 14 presents a profile $m_z^A(\Phi)$, featuring a wide plateaulike area with a small jump on the right-hand side due to system convergence to the state with a different sign of m_x.

Characteristic dependence of macrospin dynamics on $[h,\Phi]$ under a constant h_s is shown in Fig. 15. The phase diagram obtained is structurally similar to that in Fig. 12, but the regions of the in-plane precessions appear to be significantly smaller under the variation of Φ. Noncollinearity of current reveals a more pronounced boundary between the OPP limit cycles and canted states situated either to the left or to the right of the easy plane. The latter boundary is generally linear in the $[\Phi,h]$ plane for $h \gtrsim 5$. At intermediate magnetic fields, the characteristic angular dependence of the average magnetization is shown by the profile in Fig. 15, featuring a smooth plateau with a negligible notch corresponding to m_x sign changes. Magnetization reversal takes place at the angles $\Phi \approx \pm 0.4\pi$. For large applied fields [Fig. 15(b)] as well as for $h<1$, no steady precession can be triggered, and an abrupt reversal takes place for angles either

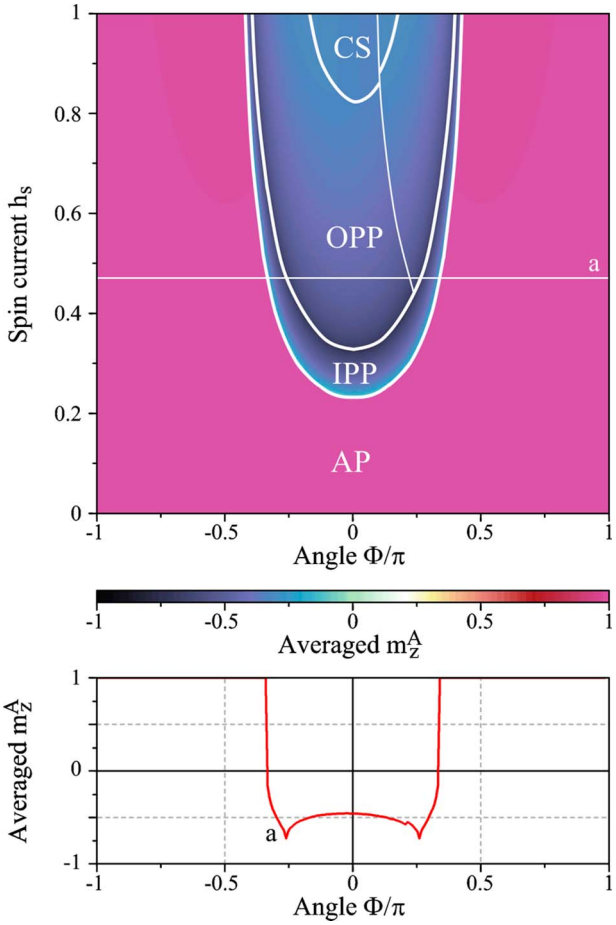

FIG. 14. (Color online) Phase diagram for the macrospin subjected to magnetic field $h=7$ and varying h_s, applied at the angle Φ with respect to the easy axis. The plot shows averaged magnetization component m_z^A (top panel) and characteristic profile along the line a at $h_s=0.47$ (bottom panel). The thin white curve dividing the OPP and CS regions corresponds to the bistability boundary, upon crossing which the sign of m_x changes.

smaller or larger than $\pi/2$, depending on the magnetic field value.

Thus, noncollinearity of the spin-current polarization vector introduces a smaller variety of changes in the macrospin dynamics. The general effect of the tilted current torque is smaller than that obtained in the collinear model, requiring, therefore, larger currents to switch the system to the desired state.

VI. ARBITRARY ORIENTATION OF MAGNETIC FIELD AND CURRENT POLARIZATION

In the most general case, both h and h_s may form arbitrary angles with the easy axis z, so the resulting macrospin dynamics can be a complicated function of h, h_s, Ψ, and Φ. In this section, we show the results of our numerical calculations performed for the pairs of current and field values corresponding to the most characteristic phase portraits shown in Figs. 3, 4, 8, and 9, investigating their transformation for $-\pi < \Psi < \pi$ and $-\pi < \Phi < \pi$. As the macrospin becomes

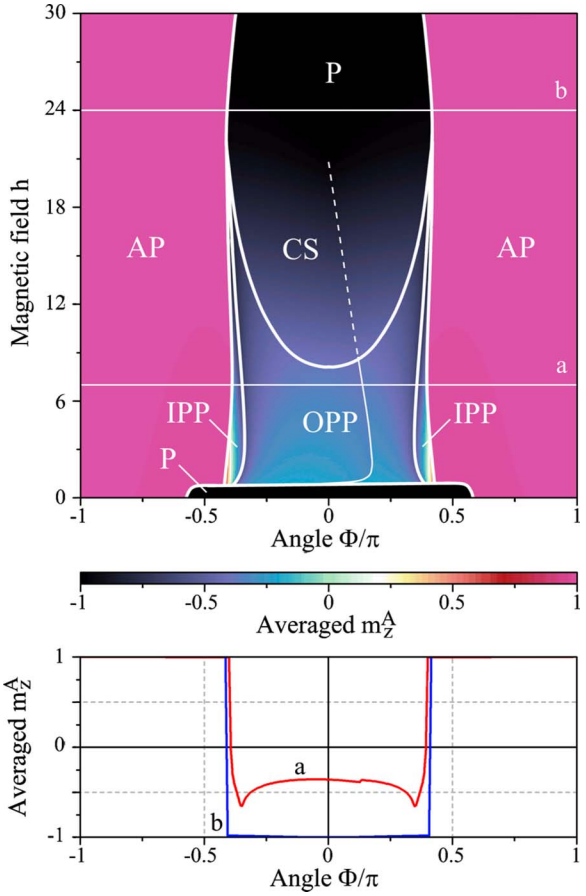

FIG. 15. (Color online) Phase diagram of macrospin states obtained for constant $h_s=0.7$, varying current noncollinearity angle Φ, and the value of magnetic field h parallel to the z axis. The thin white curve dividing the OPP region corresponds to the boundary at both sides of which magnetization is characterized with the opposite sign of m_x; the same division can be traced to the canted states, where it is marked with a dashed line. Bottom panel presents two characteristic profiles $m_z^A(\Phi)$ for the magnetic fields (a) $h=7$ and (b) $h=24$, respectively.

locked along the field or current polarization direction if the angle between h and h_s is obtuse, nontrivial dynamic states of the system can be accessible when $|\Psi-\Phi|<\pi/2$. Because of this, we have constructed the corresponding diagrams in the coordinates $[\Psi,\Psi-\Phi]$ (Fig. 16).

As one can see from the figure, proper adjustment of Ψ and Φ allows one to change the field noncollinearity in the whole range $-\pi<\Psi<\pi$, benefiting from complete switching of m_y and m_z components [Fig. 16(a)] resulting in magnetization amplitudes $\Delta m_z=2$ [Figs. 16(b) and 16(c)]. Moreover, it becomes possible to perform magnetization reversal and switching between different oscillation modes adjusting only the angles Ψ and Φ (e.g., two upper panels of Fig. 16). The latter effect may lead to important applications in spintronics as the properties of a device operating at a given current and magnetic field can be controllably changed by device rotation or by manipulating polarization direction of the spin current.

It is also noteworthy that proper fine-tuning of the angular mismatch allows one to boost the frequency of steady mac-

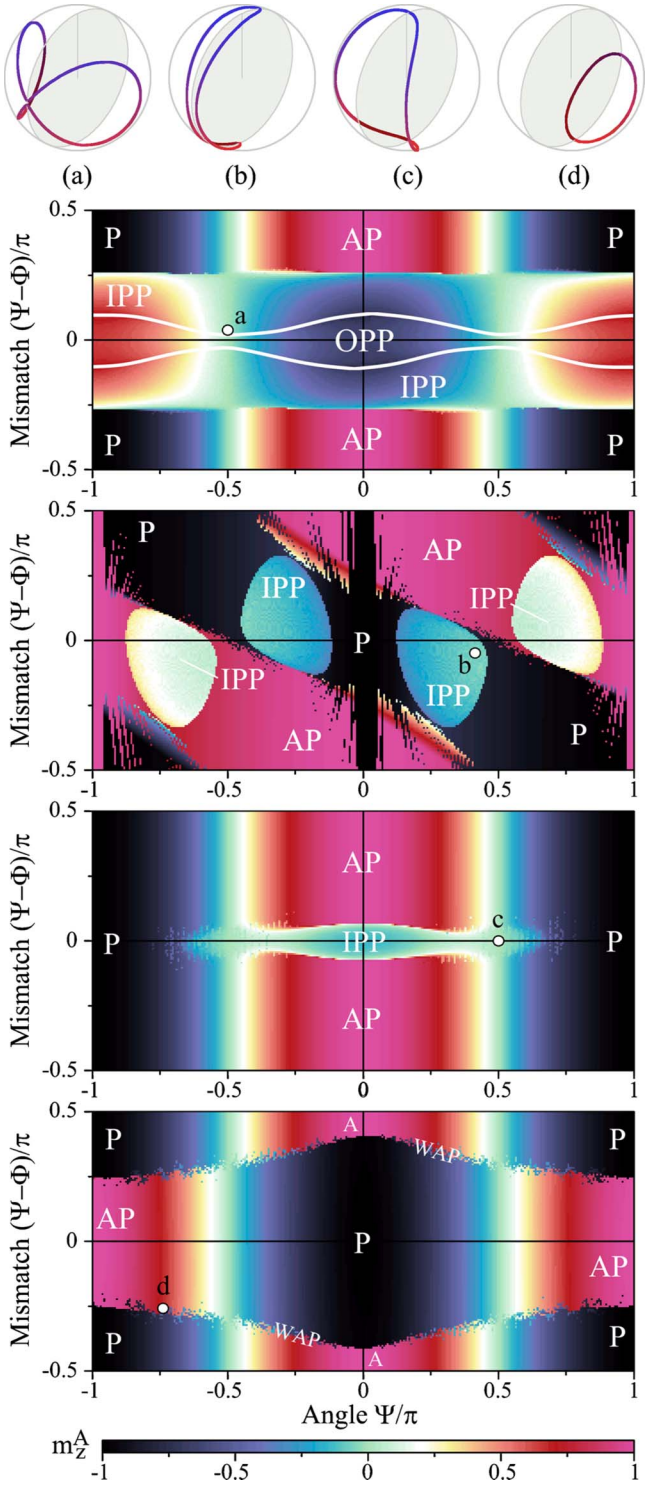

FIG. 16. (Color online) Macrospin state diagrams for arbitrary orientation of magnetic field and spin-current polarization vectors, from top to bottom: $h=7$, $h_s=0.34$; $h=0.5$, $h_s=0.235$; $h=7$, $h_s=0.235$; and $h=24.4$, $h_s=0.7$. Characteristic phase portraits are shown for (a) 90°-rotated in-plane precession similar to that shown in Fig. 3(a), $\Psi=-\pi/2$, $\Phi=1.45$; (b) ultranarrow IPP with $\Delta m_z=2$, $\Psi=1.3$, and $\Phi=1.45$; (c) wide-angle IPP with $\Delta m_z=2$, $f(m_z)=15$ GHz, $\Psi=\pi/2$, and $\Phi=\pi/2$; (d) extra-high-frequency wide-angle in-plane precession limit cycle with $\Delta m_z\approx 1$, $f(m_z)=45$ GHz, $\Psi=-2.32$, and $\Phi=-1.51$.

rospin precession up to about 45 GHz [Fig. 16(d) and bottom panel], characterized with very narrow spectral peaks and amplitude $\Delta m_z \approx 1$. The latter values represent an almost two-fold frequency increase with amplitudes, practically equal to those observed in the collinear situation. Therefore, taking into account the most general case of arbitrary alignment of applied magnetic field and injected spin-current polarization, one gets additional possibilities to control the macrospin performance, revealing various states possessing interesting and application-promising properties.

VII. CONCLUSIONS

Our simulations showed that the considerations of the macrospin dynamics based on the Landau–Lifshitz–Gilbert equation with both magnetic field and spin-current polarization vectors parallel to the easy magnetization axis lead to an oversimplification of the problem and exclude some important dynamical states of the system. In particular, a tilted magnetic field results in the rotation of the magnetic energy landscape that, in turn, causes phase trajectory rotation as well. Such tilted magnetic precession features a remapping of the magnetization components m_y and m_z, allowing one to obtain the maximum possible magnetization oscillation amplitudes of $2M_s$ along the easy magnetization axis, which is expected to render a larger signal to noise ratio for GMR measurements. For a large field noncollinearity angle Ψ, it is possible to switch the system into a wide-amplitude precession mode, characterized with the oscillation frequency exceeding 30 GHz and m_z amplitudes approaching $1.5M_s$. Moreover, large angles Ψ allow magnetization precession at lower magnetic field values $h \ll h_{\text{lower}}=1$. In this case, the magnetoresistivity response of the system is expected to be characterized with roughly square-shaped maxima centered at $\Psi \approx \pm \pi/4$. Under moderate magnetic fields, the angular dependence of the averaged magnetic component m_z is predicted to be constant in certain fixed ranges of Ψ, which can be useful for the creation of angular sensors allowing field misalignment in the desired ranges.

On the contrary, consideration of spin-current noncollinearity alone does not lead to the mentioned variety of phase states of the system. As the longitudinal component of the spin-current polarization $h_{s\|}$ becomes smaller for a larger noncollinearity angle Φ, the desired magnetic modes become obtainable under larger values of spin current. In this case, the switching threshold describing transition to the antiparallel state can be derived by a simple $h_s \rightarrow h_{s\|}$ generalization of the corresponding expressions for the collinear LLG model.

The most complete control of the macrospin dynamics is possible when both angles between h, h_s, and easy magnetization axis are considered arbitrary. By changing those angles, one can switch between different oscillation modes of the system, which is expected to render significant functionality improvements for a spintronic device, even if it operates under constant h and h_s. In particular, fine-tuning of both Ψ and Φ allows one to reach frequencies of at least 45 GHz with Δm_z amplitude about $1M_s$, which is almost twice as large as the maximum frequency attainable in the collinear mode (25 GHz, $\Delta m_z \approx 1.1M_s$). Therefore, a general noncollinear model reveals rich and interesting dynamics, predicting additional operation regimes with very important application perspectives.

ACKNOWLEDGMENTS

This work was partly supported by the FCT Grants No. POCI/FIS/58746/2004 and No. SFRH/BPD/26825/2006 in Portugal, the STCU Grant No. 3098 in Ukraine, and the funds of the Polish Ministry of Science and Higher Education as a research project for 2006–2009.

*Permanent address: Department of Physics, Adam Mickiewicz University, ulica Umultowska 85, 61-614 Poznań, Poland.

[1] I. Žutic, J. Fabian, and S. Das Sarma, Rev. Mod. Phys. **76**, 323 (2004).
[2] M. N. Baibich, J. M. Broto, A. Fert, F. Nguyen Van Dau, F. Petroff, P. Etienne, G. Creuzet, A. Friederich, and J. Chazelas, Phys. Rev. Lett. **61**, 2472 (1988).
[3] I. Kaitsu, R. Inamura, J. Toda, and T. Morita, Fujitsu Sci. Tech. J. **42**, 122 (2006).
[4] H. Kanai, K. Noma, and J. Hong, Fujitsu Sci. Tech. J. **37**, 174 (2001).
[5] J. Bass and W. P. Pratt, Jr., J. Magn. Magn. Mater. **200**, 274 (1999).
[6] K. Nagasaka, Y. Seyama, R. Kondo, H. Oshima, Y. Shimizu, and A. Tanaka, Fujitsu Sci. Tech. J. **37**, 192 (2001).
[7] J. A. Katine, F. J. Albert, R. A. Buhrman, E. B. Myers, and D. C. Ralph, Phys. Rev. Lett. **84**, 3149 (2000).
[8] S. I. Kiselev, J. C. Sankey, I. N. Krivorotov, N. C. Emley, R. J. Schoelkopf, R. A. Buhrman, and D. C. Ralph, Nature (London) **425**, 380 (2003).
[9] S. I. Kiselev, J. C. Sankey, I. N. Krivorotov, N. C. Emley, M. Rinkoski, C. Perez, R. A. Buhrman, and D. C. Ralph, Phys. Rev. Lett. **93**, 036601 (2004).
[10] S. Kaka, M. R. Pufall, W. H. Rippard, T. J. Silva, S. E. Russek, and J. A. Katine, Nature (London) **437**, 389 (2005).
[11] S. I. Kiselev, J. C. Sankey, I. N. Krivorotov, N. C. Emley, A. G. F. Garcia, R. A. Buhrman, and D. C. Ralph, Phys. Rev. B **72**, 064430 (2005).
[12] M. V. Costache, S. M. Watts, M. Sladkov, C. H. van der Wal, and B. J. van Wees, Appl. Phys. Lett. **89**, 232115 (2006).
[13] W. H. Rippard, M. R. Pufall, and S. E. Russek, Phys. Rev. B **74**, 224409 (2006).
[14] M. d'Aquino, D. Suess, T. Schrefl, C. Serpico, and J. Fidler, J. Magn. Magn. Mater. **290–291**, 506 (2005).
[15] F. B. Mancoff, R. W. Dave, N. D. Rizzo, T. C. Eschrich, B. N. Ertel, and S. Tehrani, Appl. Phys. Lett. **83**, 1596 (2003).
[16] P. Weinberger, A. Vernes, B. L. Györffy, and L. Szunyogh, Phys. Rev. B **70**, 094401 (2004).
[17] C. P. O. Treutler, Sens. Actuators, A **A91**, 2 (2001).
[18] G. Rieger, K. Ludwig, J. Hauch, and W. Clemens, Sens. Actua-

tors, A **A91**, 7 (2001).
[19] K.-M. H. Lenssen, D. J. Adelerhof, H. J. Gassen, A. E. T. Kuiper, G. H. J. Somers, and J. B. A. D. van Zon, Sens. Actuators, A **85**, 1 (2000).
[20] J. C. Slonczewski, J. Magn. Magn. Mater. **159**, L1 (1996).
[21] J. Barnas, A. Fert, M. Gmitra, I. Weymann, and V. K. Dugaev, Mater. Sci. Eng., B **126**, 271 (2006).
[22] D. V. Berkov and N. L. Gorn, J. Magn. Magn. Mater. **290–291**, 442 (2005).
[23] D. V. Berkov and N. L. Gorn, J. Appl. Phys. **99**, 08Q701 (2006).
[24] W. Scholz, J. Fidler, T. Schrefl, D. Suess, R. Dittrich, H. Forster, and V. Tsiantos, Comput. Mater. Sci. **28**, 366 (2003).
[25] M. Kružík and A. Prohl, SIAM Rev. **48**, 439 (2006).
[26] Ya. Tserkovnyak, A. Brataas, G. W. Bauer, and B. I. Halperin, Rev. Mod. Phys. **77**, 1375 (2005).
[27] I. N. Krivorotov, D. V. Berkov, N. L. Gorn, N. C. Emley, J. C. Sankey, D. C. Ralph, and R. A. Buhrman, Phys. Rev. B **76**, 024418 (2007).
[28] J. Xiao, A. Zangwill, and M. D. Stiles, Phys. Rev. B **72**, 014446 (2005).
[29] M. D. Stiles and J. Miltat, in *Spin Dynamics in Confined Magnetic Structures III*, Topics in Applied Physics Vol. 101, edited by B. Hillebrands and A. Thiaville (Springer, Berlin, 2006).
[30] J. Z. Sun, Phys. Rev. B **62**, 570 (2000).
[31] Ya. B. Bazaliy, B. A. Jones, and S. C. Zhang, Phys. Rev. B **69**, 094421 (2004).
[32] H. Morise and S. Nakamura, Phys. Rev. B **71**, 014439 (2005).
[33] R. Bonin, G. Bertotti, I. D. Meyergoyz, and C. Serpico, J. Appl. Phys. **99**, 08G508 (2006).
[34] J. Grollier, V. Cros, and A. Fert, Phys. Rev. B **73**, 060409(R) (2006).
[35] M. d'Aquino, G. Bertotti, C. Serpico, I. D. Mayergoyz, and R. Bonin, IEEE Trans. Magn. **42**, 3195 (2006).
[36] S. E. Russek, S. Kaka, W. H. Rippard, M. R. Pufall, and T. J. Silva, Phys. Rev. B **71**, 104425 (2005).
[37] M. Belmeguenai, T. Devolder, and C. Chappert, J. Phys. D **39**, 1 (2006).
[38] Q. Mistral, J.-V. Kim, T. Devolder, P. Crozat, C. Chappert, J. A. Katine, M. J. Carey, and K. Ito, Appl. Phys. Lett. **88**, 192507 (2006).
[39] Z. Z. Sun and X. R. Wang, Phys. Rev. B **71**, 174430 (2005).
[40] P. M. Gorley, P. P. Horley, V. K. Dugaev, J. Barnaś, and W. Dobrowolski, J. Appl. Phys. **101**, 034504 (2007).
[41] Ya. B. Bazaliy, B. A. Jones, and S. C. Zhang, Phys. Rev. B **57**, R3213 (1998).
[42] Ya. B. Bazaliy, B. A. Jones, and S. C. Zhang, J. Appl. Phys. **89**, 6793 (2001).
[43] Ya. B. Bazaliy and B. A. Jones, Physica B (Amsterdam) **329–333**, 1290 (2003).
[44] Ya. B. Bazaliy, Phys. Rev. B **76**, 140402(R) (2007).
[45] M. Gmitra and J. Barnaś, Appl. Phys. Lett. **89**, 223121 (2006).
[46] R. Bonin, C. Serpico, G. Bertotti, I. D. Meyergoyz, and M. d'Aquino, Eur. Phys. J. B **59**, 435 (2007).
[47] A. J. Lichtenberg and M. A. Lieberman, *Regular and Stochastic Dynamics* (Springer, New York, 1992).
[48] H. Xi and Z. Lin, Phys. Rev. B **70**, 092403 (2004).
[49] J. Sun, Nature (London) **425**, 359 (2003).
[50] S. Urazhdin, R. Loloee, and W. P. Pratt, Jr., Phys. Rev. B **71**, 100401(R) (2005).